

Article

A Study of the CO Sensing Responses of Cu-, Pt- and Pd-Activated SnO₂ Sensors: Effect of Precipitation Agents, Dopants and Doping Methods

Venkata Krishna Karthik Tangirala ^{1,*}, Heberto Gómez-Pozos ², Ventura Rodríguez-Lugo ³ and María De La Luz Olvera ¹

¹ Departamento de Ingeniería Eléctrica-SEES, Centro de Investigación y de Estudios Avanzados del Instituto Politécnico Nacional, CINVESTAV-IPN, Apartado postal 14740, México D. F. 07360, Mexico; molvera@cinvestav.mx

² Área Académica de Computación y Electrónica, ICBI, Universidad Autónoma del Estado de Hidalgo, Hidalgo 56092, Mexico; gpozos@uaeh.edu.mx

³ Área Académica de Ciencias de la Tierra y Materiales, Instituto de Ciencias Básicas e Ingeniería, Universidad Autónoma del Estado de Hidalgo, Carretera Pachuca-Tulancingo Km. 4.5, Hidalgo 42184, Mexico; ventura.rl65@gmail.com

* Correspondence: krishnakarthik.tv@gmail.com; Tel.: +52-553-194-7927

Academic Editor: Giovanni Neri

Received: 27 February 2017; Accepted: 27 April 2017; Published: 3 May 2017

Abstract: In this work, we report the synthesis of Cu, Pt and Pd doped SnO₂ powders and a comparative study of their CO gas sensing performance. Dopants were incorporated into SnO₂ nanostructures using chemical and impregnation methods by using urea and ammonia as precipitation agents. The synthesized samples were characterized using X-ray diffraction (XRD), Raman spectroscopy, scanning electron microscopy (SEM) and high resolution transmission electron microscopy (HR-TEM). The presence of dopants within the SnO₂ nanostructures was evidenced from the HR-TEM results. Powders doped utilizing chemical methods with urea as precipitation agent presented higher sensing responses compared to the other forms, which is due to the formation of uniform and homogeneous particles resulting from the temperature-assisted synthesis. The particle sizes of doped SnO₂ nanostructures were in the range of 40–100 nm. An enhanced sensing response around 1783 was achieved with Cu-doped SnO₂ when compared with two other dopants i.e., Pt (1200) and Pd:SnO₂ (502). The high sensing response of Cu:SnO₂ is due to formation of CuO and its excellent association and dissociation with adsorbed atmospheric oxygen in the presence of CO at the sensor operation temperature, which results in high conductance. Cu:SnO₂ may thus be an alternative and cost effective sensor for industrial applications.

Keywords: tin oxide pellets; doping; HRTEM analysis; CO; sensing response

1. Introduction

Gas leak detection is a constructive testing method for dangerous combustible gases [1]. Carbon monoxide (CO) is a toxic hazardous industrial gas produced from the incomplete burning of all carbon-based fuels. Different kinds of materials including metal oxide semiconductors (MOSs) are employed for detecting CO [2–8]. As Wagner discovered [9], atoms and molecules adsorbed on the MOS surface influence its conductivity. Among the available MOS materials, SnO₂ is usually considered to be one of the best candidates for developing gas sensors due to its relatively low cost of production and adequate oxygen vacancies [10,11].

Commercially available SnO₂ gas sensors are mainly in the form of thick or thin films or pellets [12,13]. Despite having disadvantages like high power consumption, low temperature homogeneity and low

electrode efficiency in collecting the free charge carriers, pellets are more viable for gas sensors due to their high porosity, abundant material, no substrate effects and they can serve as reference values for comparing thin or thick film sensors. Dopants in MOS materials improve the surface reactivity with atmospheric oxygen and subsequently the sensing response by residing on the surface in the form of metal clusters or by modifying the crystalline structure [14,15]. For gas sensing applications, the major catalytically active doping additives are noble metals (Pd, Pt, etc.), and transition metals (Cu, Fe, etc.) [16–18]. In general transition metals serve as “accelerators” of various processes [19] and noble metals serve as “catalysts” and also decrease the sensor operation temperature [20]. Platinum (Pt) and palladium (Pd) are the most used dopants due to their chemical inertness and higher work function (~5.8 and ~5.4 eV, respectively) than the band gap (3.6 eV) of SnO₂ [21–25]. On the other hand, copper (Cu) is the most used transition metal for doping due its comparable ionic radius as tin. The radii of Sn⁴⁺ and Cu²⁺ are around 0.71 and 0.72 Å, respectively [26]. The association of Cu with atmospheric oxygen and its dissociation with CO at elevated temperatures also improves the surface conductivity of Cu-doped SnO₂ pellets [27].

Different methods like flame spray [28], sol-gel [29], microwave irradiation [30], and wet chemical synthesis [31] are reported for the preparation of SnO₂ powders. Among others, wet chemical synthesis employing urea as precipitant agent requires a moderate temperature (80–100 °C) which provides coarse powders with adequate characteristics to be used in gas sensing applications [32]. Another key factor that affects the sensing response is the dopant concentration. Many previous works about doping concentration effects reason that the sensing response increases with the increase in the doping concentration due to the corresponding increase in catalytical activity [26,27]. In this work, a study of dopant concentration effect is obviated due to the consideration of adequate variables like precipitation agent—urea and ammonia, dopant type—Cu, Pt and Pd and doping method—chemical doping and impregnation methods. In our future work these sensors will be tested for different dopant concentrations for different gas atmospheres to obtain selectivity and stability.

In this work, SnO₂ pellets doped with 1 wt % Cu, Pt and Pd, were synthesized by wet chemical synthesis using urea and ammonia as a precipitation agents. Ammonia was employed to observe the effect of precipitation agent in the particle size. Additionally, two methods were employed for the incorporation of the dopants Cu, Pt and Pd, namely, chemical doping and the impregnation method. Cu-doped SnO₂ pellets show excellent gas response to CO as comparison Pt- and Pd-doped SnO₂ pellets using both doping methods. Simultaneously, the structural, morphological characterizations and their corresponding calculations provide a clear and deep perception of the effects of the dopant on the sensing properties of SnO₂. Our study thus represents a viable way for understanding the effect of dopants on the SnO₂ gas sensors.

2. Materials and Methods

2.1. Preparation of Former Pure SnO₂ Powders Using Urea and Ammonia

Feedstock solution was prepared by mixing 0.4 M aqueous tin chloride pentahydrate (SnCl₄·5H₂O; J. T. Baker, Mexico City, Mexico) and urea (CH₄N₂O; Sigma Aldrich, Mexico City, Mexico) in 1:2 ratio. Then the mixed solution was vigorously stirred and heated until the solution temperature reaches around 93 ± 5 °C. Unlike the former case (urea), for ammonia (NH₄OH; Sigma Aldrich) as precipitation agent it was added dropwise to 0.4 M aqueous SnCl₄·5H₂O until the pH of the solution reached 12. The resultant precipitates in both cases were centrifuged at 400 rpm for 1 h using a ROTINA-420R centrifuge (Hettich, Toluca, Mexico) and the obtained pastes were dried at 100 °C for 24 h to eliminate any remaining solvent. Finally, the dried powders were calcined in a furnace at 800 °C for 2 h to obtain pure SnO₂ powders. All the synthesis conditions were studied, optimized and reported in our previous works [33,34].

2.2. Preparation of Chemical Doped SnO₂ Powders

One wt % aqueous CuCl₂ (Sigma Aldrich) was added to a previously prepared stock solution (0.4 M aqueous SnCl₄·5H₂O and CH₄N₂O in 1:2 ratio). Then a procedure similar to the one explained in Section 2.1 was followed to obtain Cu-doped SnO₂ powders (Cu:SnO₂) utilizing urea and ammonia as precipitation agents. Similarly, Pt:SnO₂ and Pd:SnO₂ powders were prepared utilizing PtCl₂ and PdCl₂, respectively.

2.3. Preparation of Impregnated SnO₂ Powders

Primarily, 1 g each of the previously obtained (refer to Section 2.1) pure SnO₂ powders utilizing the precipitation agents urea and ammonia were considered. Subsequently, these powders were separately impregnated with 1 wt % aqueous solutions of dopant chlorides, CuCl₂, PtCl₂ and PdCl₂ (Sigma Aldrich). All the impregnated powders were annealed at 350 °C for 2 h in air to remove the residual species. A summary of all the samples obtained by the different doping methods and using the different precipitation agents is listed in Table 1. Pellets were manufactured from all the obtained Cu-, Pt- and Pd- doped SnO₂ powders by using a manual pressing machine. The optimal pressing conditions, determined after several trials, were 16 tons applied for 90 min.

Table 1. List of samples with their corresponding doping methods and precipitation agents employed.

Name of the Sample	Doping Method	Precipitation Agent	Dopant
Cu:SnO ₂ _U_Chem	Chemical doping	Urea	Cu
Cu:SnO ₂ _A_Chem	Chemical doping	Ammonia	
Cu:SnO ₂ _U_Impe	Impregnation	Urea	
Cu:SnO ₂ _A_Impe	Impregnation	Ammonia	
Pt:SnO ₂ _U_Chem	Chemical doping	Urea	Pt
Pt:SnO ₂ _A_Chem	Chemical doping	Ammonia	
Pt:SnO ₂ _U_Impe	Impregnation	Urea	
Pt:SnO ₂ _A_Impe	Impregnation	Ammonia	
Pd:SnO ₂ _U_Chem	Chemical doping	Urea	Pd
Pd:SnO ₂ _A_Chem	Chemical doping	Ammonia	
Pd:SnO ₂ _U_Impe	Impregnation	Urea	
Pd:SnO ₂ _A_Impe	Impregnation	Ammonia	

2.4. Characterization

X-ray diffraction analysis using a PANalytical diffractometer (Panalytical, Mexico City, Mexico) with CuK α at 20 mA and 40 kV was carried out to identify the phase compounds, crystallite size, lattice parameters and the crystalline structure of the doped SnO₂ powders. Raman scattering spectroscopy of pure and doped SnO₂ powders were analyzed using 532 nm laser beams and detecting scattering signals by a thermoelectrically cooled charge coupled detector.

Scanning electron microscopy (SEM), using an AURIGA instrument (Zesis, Mexico City, Mexico), was employed to examine the morphological characteristics and the particle size of the calcined agglomerates. Additionally, SEM was also employed to analyze the surface morphological characteristics of all synthesized powders. A high resolution transmission electron microscope (HRTEM, JEM-ARF 200F, JEOL, Mexico City, Mexico) was employed to identify the dopants; additionally crystallite size, crystal planes and the lattice spacing between the SnO₂ crystal planes were estimated.

For CO sensing measurements, pure silver ohmic contacts were deposited on the pellets surface by the thermal evaporation technique. The experimental setup for measuring the electrical resistance of the pellets is shown in Figure 1. The measurements were made at three different operating temperatures, namely 100, 200, and 300 °C. Lower operation temperatures (<100 °C) do not lead to conductance changes. The conductance changes were registered by using a Keithley 2001 multimeter (Keithley,

Mexico City, Mexico). For controlling the partial pressure in the chamber a TM20 detector (Leybold, Mexico City, Mexico) was used. The sensing response of the pellets, $S = R_{air}/R_{gas}$, was obtained by calculating the electrical conductance ratio from the measured resistance in air, R_{air} , and in the presence of different concentrations of CO, 1, 5, 50, 100, 200 and 300 ppm, R_{gas} .

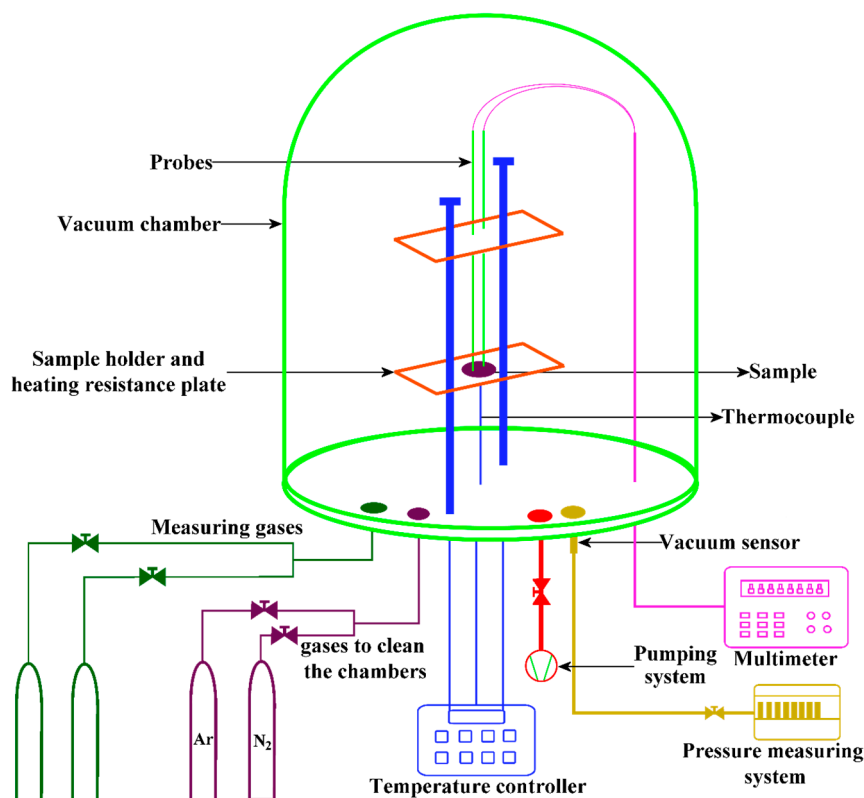


Figure 1. Schematic diagram of the homemade gas sensing system.

3. Results

3.1. X-ray Diffraction Analysis

In this work, doped SnO₂ nanocrystals were synthesized under various conditions involving different precipitation agents, dopants and doping methods. Figure 2a–c depict the XRD patterns obtained for Cu, Pt and Pd:SnO₂ powders respectively in comparison with pure SnO₂ XRD patterns. Irrespective of the precipitation agent and doping method, it is evident from these figures that all the doped-SnO₂ powders exhibit the tetragonal rutile phase of SnO and SnO₂, matching the JCPDS cards 06-0395 and 77-0450, respectively [35], whereas, undoped powders demonstrate pure SnO₂ peaks, and no additional SnO₂ phases were found. Therefore, the simultaneous presence of SnO and SnO₂ in all doped powders leads to the conclusion that the dopants reduce the SnO₂ crystallinity and inhibit the further oxidation of the SnO to SnO₂, and intergrowth mechanisms may occur at a thermal oxidizing temperature of 800 °C [36].

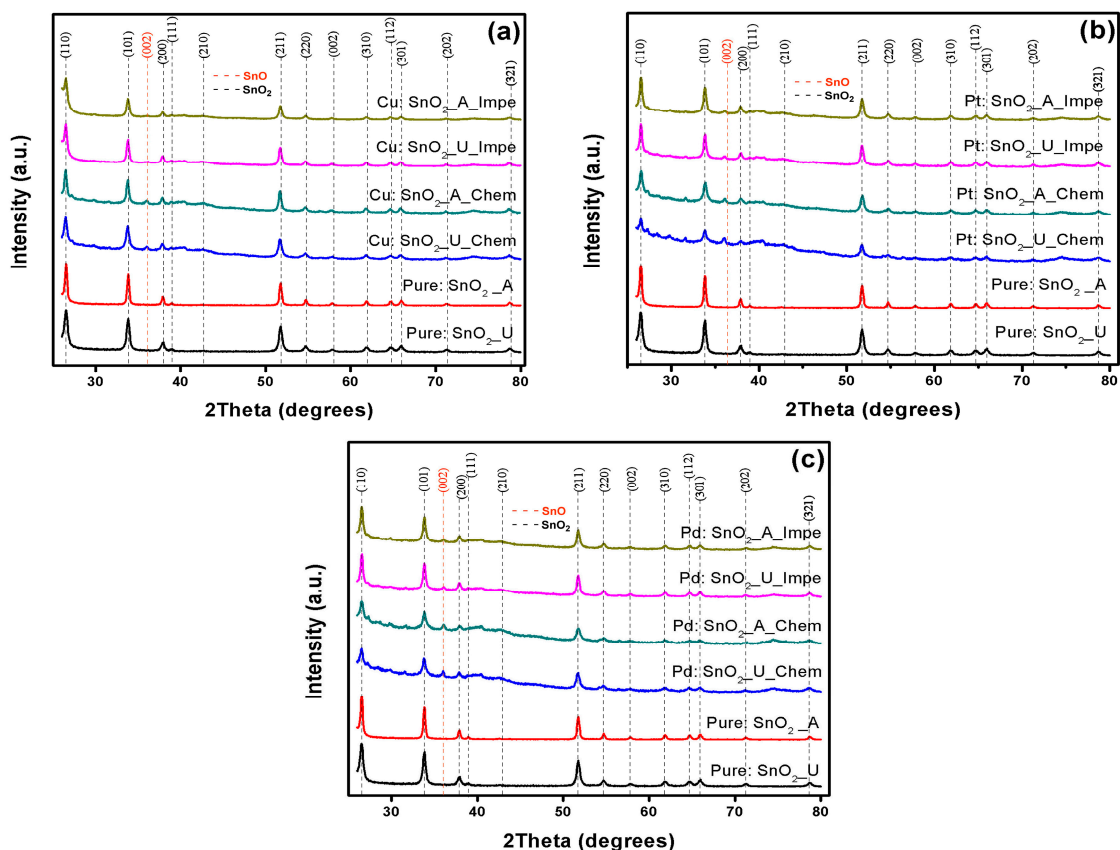


Figure 2. XRD patterns of (a) Cu:SnO₂; (b) Pt:SnO₂; and (c) Pd:SnO₂ powders for different precipitation agents and doping methods.

No additional peaks corresponding to Cu, Pt and Pd are found in the XRD spectra, which can be due to two reasons. First, the doping concentration is 1 wt %, which is very low to detect any changes with the X-ray diffractometer, this affirms a partial incorporation of dopants into the crystal lattice, whereas others can be in form of clusters. Secondly, total incorporation of all dopants into the SnO₂ crystal lattice in all the doping cases also results an absence of dopant peaks. An upshift and additional peaks were observed in all the doped powders which is corroborated by the decrease in the SnO₂ crystal quality, and these discrepancies are much higher for Pt and Pd:SnO₂ as compared to Cu:SnO₂ powders. The amount of crystal discrepancies is proportional to the ionic radii of the dopants (the ionic radii of Sn²⁺, Cu²⁺, Pt²⁺ and Pd²⁺ are 0.71, 0.73, 0.80 and 0.86 Å, respectively) [26,27].

Figure 3a–c show the shift in the SnO₂ preferential orientation plane (110) of the Cu, Pt and Pd:SnO₂ samples, respectively. Irrespective of the dopant utilized (Cu, Pt or Pd), the chemically doped powders shift slightly to a higher angle compared to impregnated powders. A left shift with peak broadening was observed for Cu:SnO₂ powders (Figure 3a), while on the contrary a right shift is evidenced for Pt:SnO₂ and Pd:SnO₂ (Figure 3b,c). This clearly evidences that the incorporated dopants cause a strain in the SnO₂ crystals which results in a planar stress. The shift to a lower angle for Cu:SnO₂ powders corresponds to a compressive stress and those to a higher angle for the Pt, Pd:SnO₂ powders represents a tensile stress [26,27].

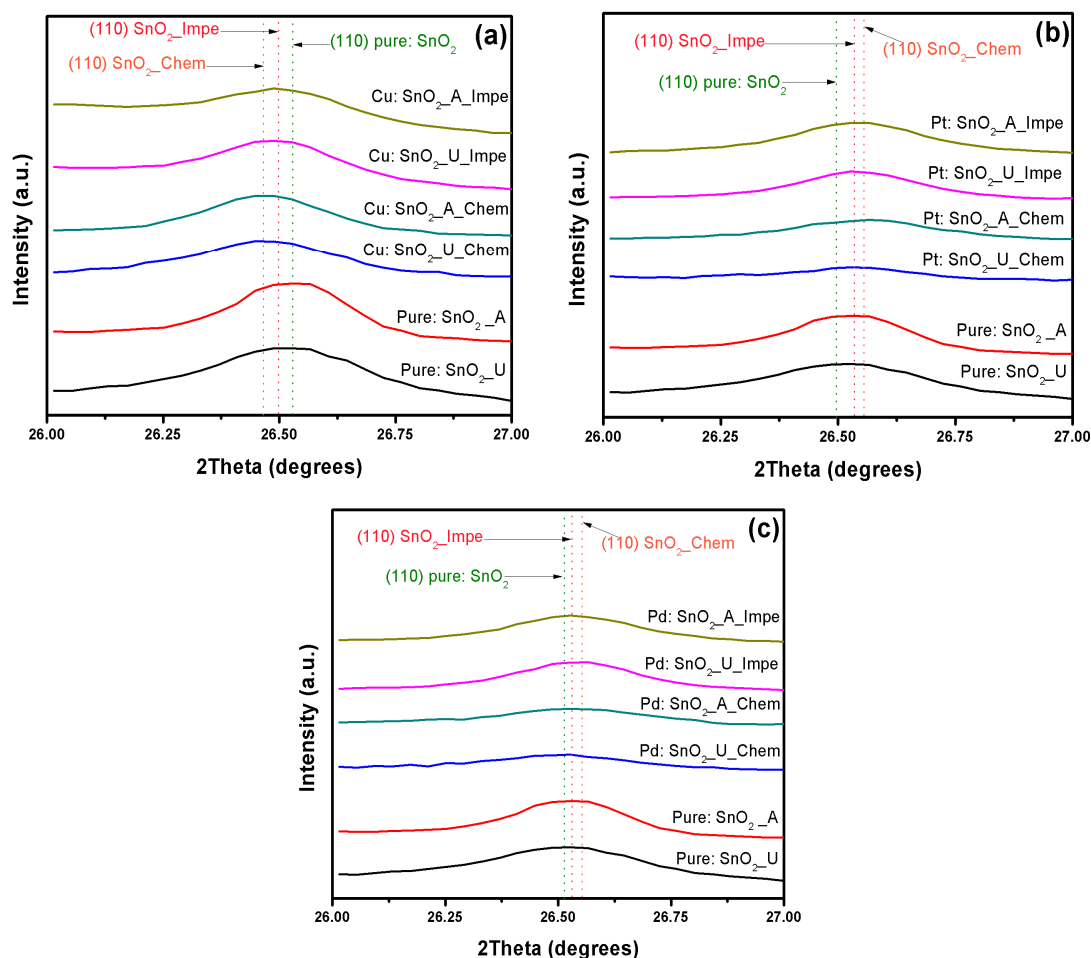


Figure 3. (110) plane shift and peak broadening of (a) Cu:SnO₂; (b) Pt:SnO₂; and (c) Pd:SnO₂ powders for different precipitation agents and doping methods.

In order to ascertain the effect of dopants (Cu, Pt and Pd) on the structural characteristics, crystallite size (D) [37], crystal volume (V) [38] and porosity (P) [39] are calculated from Equations (1)–(5) and reported in Table 2.

$$D = \frac{0.89\lambda}{\beta \cos\theta} \quad (1)$$

$$V = a^2c \quad (2)$$

$$P = \left(1 - \frac{\rho_a}{\rho_x}\right) \times 100\% \quad (3)$$

$$\rho_a = \frac{m}{v} \quad (4)$$

$$\rho_x = \frac{nM}{NV} \quad (5)$$

where λ is the wavelength of the incident X-rays ($\lambda = 0.15418$ nm), β is the full width half maximum (FWHM) intensity, θ is the Bragg's diffraction angle in radians, a and c are lattice parameters, m and v are mass and volume of the samples, n is number of molecules per unit cell, M is the molecular weight and N is Avogadro's number.

Table 2. Crystallite size (D); Volume of the crystal (V); and Porosity (P) of the Cu, Pt and Pd-SnO₂ nano crystals.

Sample Name	D (nm)	V (10 ⁻²⁴ cm ³)	P (%)
SnO ₂ _U	26.3	71.4	32.3
SnO ₂ _A	30.0	71.6	32.4
Cu:SnO ₂ _U_Chem	21.2	71.7	58.4
Cu:SnO ₂ _A_Chem	21.0	71.7	58.5
Cu:SnO ₂ _U_Impe	22.2	71.7	58.5
Cu:SnO ₂ _A_Impe	22.0	71.8	58.7
Pt:SnO ₂ _U_Chem	35.0	71.8	64.6
Pt:SnO ₂ _A_Chem	35.0	71.8	64.7
Pt:SnO ₂ _U_Impe	33.0	71.8	64.8
Pt:SnO ₂ _A_Impe	33.0	71.9	64.8
Pd:SnO ₂ _U_Chem	42.0	72.0	73.0
Pd:SnO ₂ _A_Chem	42.0	72.0	73.0
Pd:SnO ₂ _U_Impe	40.0	72.0	73.0
Pd:SnO ₂ _A_Impe	40.0	72.2	73.2

From Table 2 it can be observed that, for Cu:SnO₂ powders, the crystallite sized decreased (a left shift, compressed stress; Figure 3) from 26 to 21 nm, whereas for Pt and Pd:SnO₂ powders crystallite size increased (a right shift, tensile stress; Figure 3) from 26 to ~35 and 42 nm, respectively. These crystallite size changes are in good agreement with the peak shifts observed in Figure 3. The SnO₂ crystallite size of chemically doped powders decreased more with Cu doping and increased more for Pt and Pd dopants, compared to impregnated powders. The higher ionic radii of Pt and Pd compared to Sn results in a tensile stress and increase in SnO₂ crystallite size for Pt, Pd:SnO₂ powders [40]. The presence of Cu inhibited further SnO₂ growth and decreases the crystallite size, whereas seeing compressed stress for Cu:SnO₂ powders is puzzling. A linear relation is noticed between the volume of the unit cell and porosity and is apparent because doping with an atom with higher ionic radius increases the volume of the unit cell and subsequently porosity. No significant effects of precipitation agent (urea/ammonia) on structural properties were observed.

3.2. Raman Analysis

To confirm the effect of precipitation agent and doping method on the SnO₂ nanoparticles' growth, Raman spectroscopy measurements were carried out. It is well known that SnO₂ has a tetragonal structure with six atoms (two Sn and four O) per unit cell [41]. The 6-unit cell atoms give a total of 18 branches for the vibrational modes in the first Brillouin zone. The mechanical representation of the normal vibration modes, all the vibrational modes of SnO₂ with corresponding Raman shift peaks were also widely known and reported by various authors [42–44]. Table 3 summarizes the different frequencies of the optical modes of SnO₂, with the corresponding vibrational directions.

Table 3. Raman, IR and other vibrational modes of SnO₂.

Modes	Notation	Direction of Vibration with Respect to c-Axis	Raman Shift (cm ⁻¹)
Raman active	A _{1g}	Perpendicular	638
	B _{1g}	Perpendicular	100
	B _{2g}	Perpendicular	782
	E _g	Parallel	476
IR active	A _{2u}	Parallel	705
	E _u	Perpendicular	244
Silent	A _{2g}	Perpendicular	398
	B _{1u}	Parallel	140

The Raman spectra of Cu, Pt and Pd:SnO₂ synthesized by different doping methods are shown in Figure 4a,b. One IR active and three Raman active modes were observed at 255.2, 482.8, 637.6 and 779.2 cm⁻¹, corresponding to the E_u, E_g, A_{1g}, and B_{2g} vibration modes of SnO₂, respectively, corresponding in turn to the bulk rutile SnO₂ [45]. The intensity of the Raman peaks denotes the amount of extraction and compression of Sn-O bonds in the lattice [46]. It is interesting to note that the Cu doping decreases the intensities of Raman peaks (Figure 4a) which is corroborated by the Sn-O disorders arising due to Cu incorporation in the SnO₂ lattice.

From Figure 4a, it can also be observed that the intensities of the A_{1g} Raman peak were much less for powders synthesized with ammonia as precipitation agent. The rate of decrease in the A_{1g} peak intensity is higher for chemically doped powders than impregnated ones. No peak shifts were observed from the Raman spectra, and the minimum amount of doping percentage for observing a peak shift in Raman spectra was around 3 wt % [43–45].

Figure 4b shows a comparison of the Raman spectra of chemically doped Cu, Pt and Pd:SnO₂ with urea as precipitation agent. Cu:SnO₂ doped powders present higher intensities than Pt and Pd:SnO₂ powders which is correlated to the ionic radii of the dopant ions. As Pd has a higher ionic radius compared to Pt and Cu, it causes higher Sn-O disorders in the lattice, which makes the intensities of Pd:SnO₂ powders diminish. The effect of grain size on the Raman intensities is explained in detail in the upcoming SEM analysis (Section 3.3).

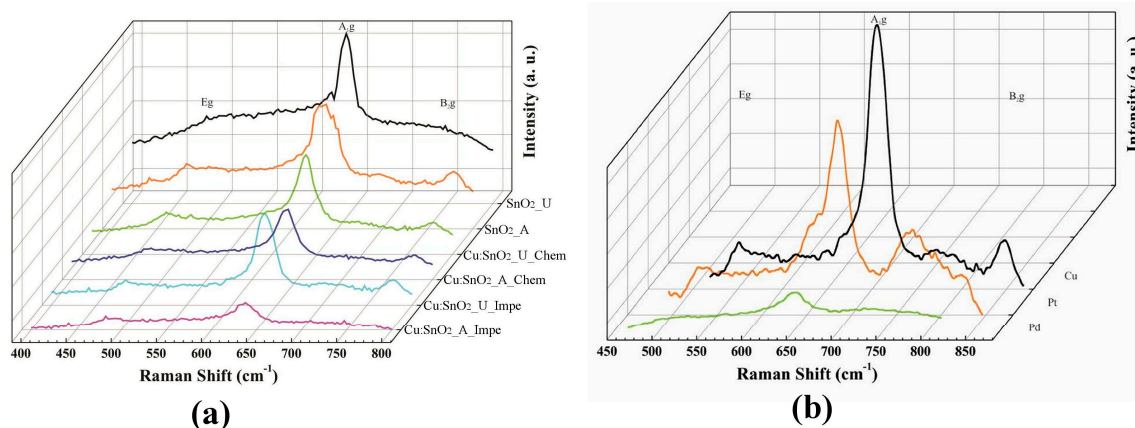


Figure 4. Raman spectra of the (a) Cu:SnO₂ with different doping methods; and (b) Cu, Pt and Pd:SnO₂ using chemical doping with urea as precipitation agent.

3.3. SEM Analysis

SEM was employed to further examine and interpret the morphologies and structures of the powders with respect to the precipitation agent and dopant methods. Figure 5a–d show representative SEM images of Cu:SnO₂_U_Chem, Cu:SnO₂_A_Chem, Cu:SnO₂_U_Impe, Cu:SnO₂_A_Impe, respectively. The observed average diameters of the Cu:SnO₂ nanoparticles are in the 25–35 nm range.

From Figure 5, powders that are chemically doped (Figure 5a,b) shows a contact area between particles, which are the necks between grains. The additives which are added during the synthesis process are incorporated into the lattice of the metal oxide, which further inhibits the grain size [47] and promotes coalescence during the heat treatment. This later coalescence leads to the formation of necks between the grains [48], which in turn influence the bulk conductivity and the thickness of the space charge region. On the other hand, impregnated powders (Figure 5c,d) show only an agglomeration between the particles, the additives which are impregnated on the thermally treated SnO₂ powders which does not promote the coalescence.

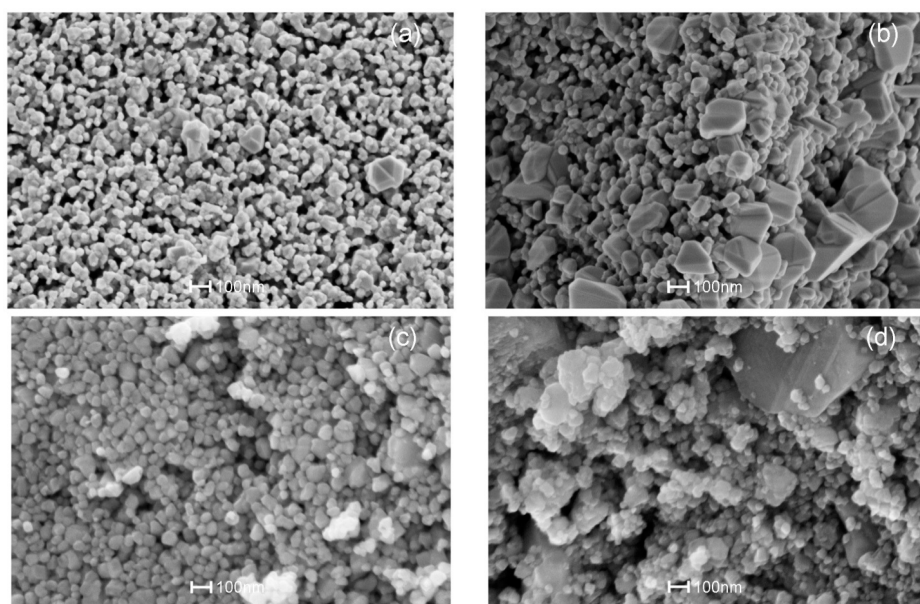


Figure 5. SEM images of Cu:SnO₂ powders using chemical doping with precipitation agent (a) urea, (b) ammonia and Cu impregnated SnO₂ powders with precipitation agent (c) urea, (d) ammonia.

From Figure 5b,d, it is also evident that larger crystals around 200–600 nm in size were observed for the powders with ammonia as precipitation agent in addition to the SnO₂ nanoparticles. The formation of larger crystals is due to the rapid precipitation at room temperature. In the case of powders precipitated using urea (Figure 4a,c), the elevated temperature of around 90 °C utilized for decomposing the urea also resulted in homogenous precipitation [49]. This in turn resulted in a relatively uniform particle size of around 20 nm and similar behavior was noticed for the Pt and Pd:SnO₂ powders (Figure 6). Figure 6a–d show representative SEM images of Pt:SnO₂ and Pd:SnO₂ powders obtained by chemical doping and impregnation, respectively.

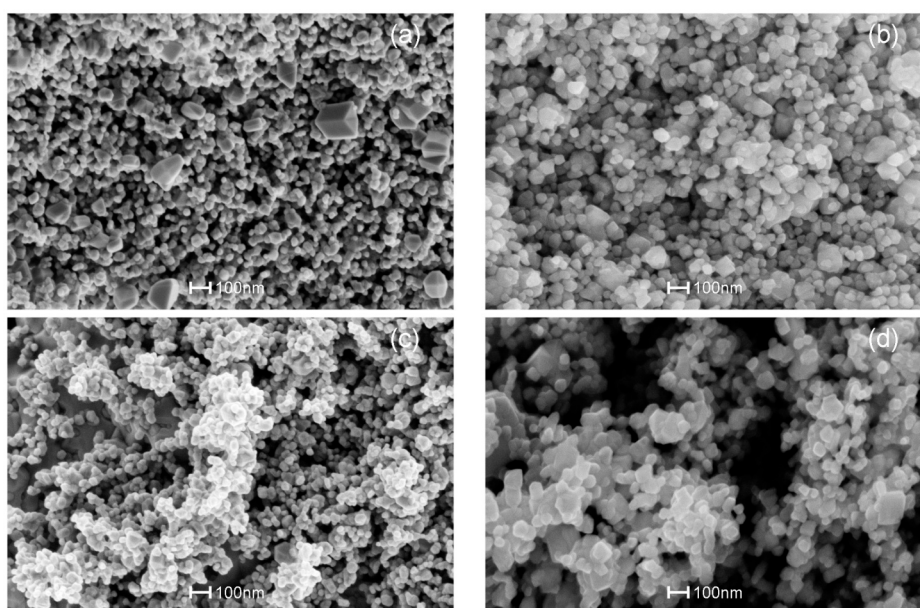


Figure 6. SEM images of (a,b) Pt:SnO₂ and (c,d) Pd:SnO₂ powders using chemical doping with (a,c) urea and (b,d) ammonia as precipitation agents.

Like the Cu:SnO₂ powders, Pt and Pd:SnO₂ powders also shows necks between the grains for the chemically doped ones (Figure 6a,c). The average diameters of the observed Pt and Pd:SnO₂ nano-particles are around 45 and 60 nm, respectively. The structures shown in Figure 5 correspond to Cu:SnO₂, whereas the structures shown in Figure 6 corresponds to Pt and Pd:SnO₂ powders, whose particle and grain sizes are relatively larger than the former ones. This increase is corroborated to the collection of grain boundaries by the additives due to the interfacial tension [47]. It is well known that the lower interfacial tension involves less energy in formation of a surface, which subsequently gives lower size grains [47–49]. Pt and Pd need a higher interfacial tension due to their higher ionic charge compared to copper [48], which results in more disorder in Pt- and Pd-doped SnO₂ structures, as evidenced by the Raman analysis (Figure 4b). From the Raman analysis (Figure 4b), we can observe that the Cu:SnO₂ powders show higher Raman intensities than Pt and Pd:SnO₂ powders, corresponding to a lower Sn-O disorder. From Figures 5 and 6, we can conclude that the chemically doped powders are favorable to promote gas sensing because the conductivity increases due to the formation of necks between the grains [50].

Porosity is another important factor that affects the sensing response [51]. It has already been reported [52,53] that the SnO₂ sensing response increases with respect to the porosity with different additives. An increment in the surface porosity will increase the active surface area which allows the sensing gas to diffuse into the pellet pores [54]. To observe the pellet surface porosity, chemically doped Cu:SnO₂ powders were observed by SEM at a lower magnification and the results are shown in Figure 7. The porous surface has a mesh-like morphology due to the smaller particle size and formation of necks between the particles.

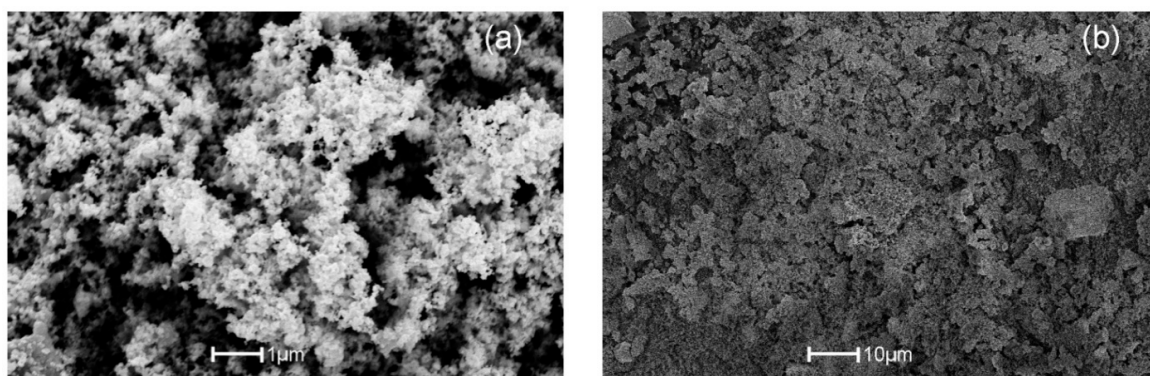


Figure 7. SEM images of Cu:SnO₂ using chemical doping with urea as precipitation agent at (a) 1 μm; and (b) 10 μm scales.

3.4. HRTEM Analysis

To obtain more-detailed structural information the Cu-, Pt- and Pd-doped SnO₂ particles were analyzed by HRTEM. Figure 8 shows the Cu:SnO₂ particles prepared by chemical doping (a) and impregnation (b). The powders are composed of agglomerated nanometric crystals around 25–30 nm in size, which is in good agreement with the XRD results.

Magnified views of Figure 8a,b are shown in Figure 8c,d and their corresponding reconstructed images are shown in Figure 8e,f, respectively. The insets in Figure 8e,f are the corresponding selected-area electron diffraction (SAED) patterns. The differences in the effects of the doping method (chemically doped/impregnated) are remarkable. In the case of the chemically doped sample, all the atomic planes are well defined and correspond to SnO₂ crystals (Figure 8c) and its surface is free from any dopants, unlike for impregnated powders (Figure 8d). The *d*-spacings measured from SAED are in good agreement with those of the (110) plane of cassiterite SnO₂ (JCPDS Card 77-0450 card) [35], corresponding to the tetragonal crystal structure (space group = *P42/mnm*).

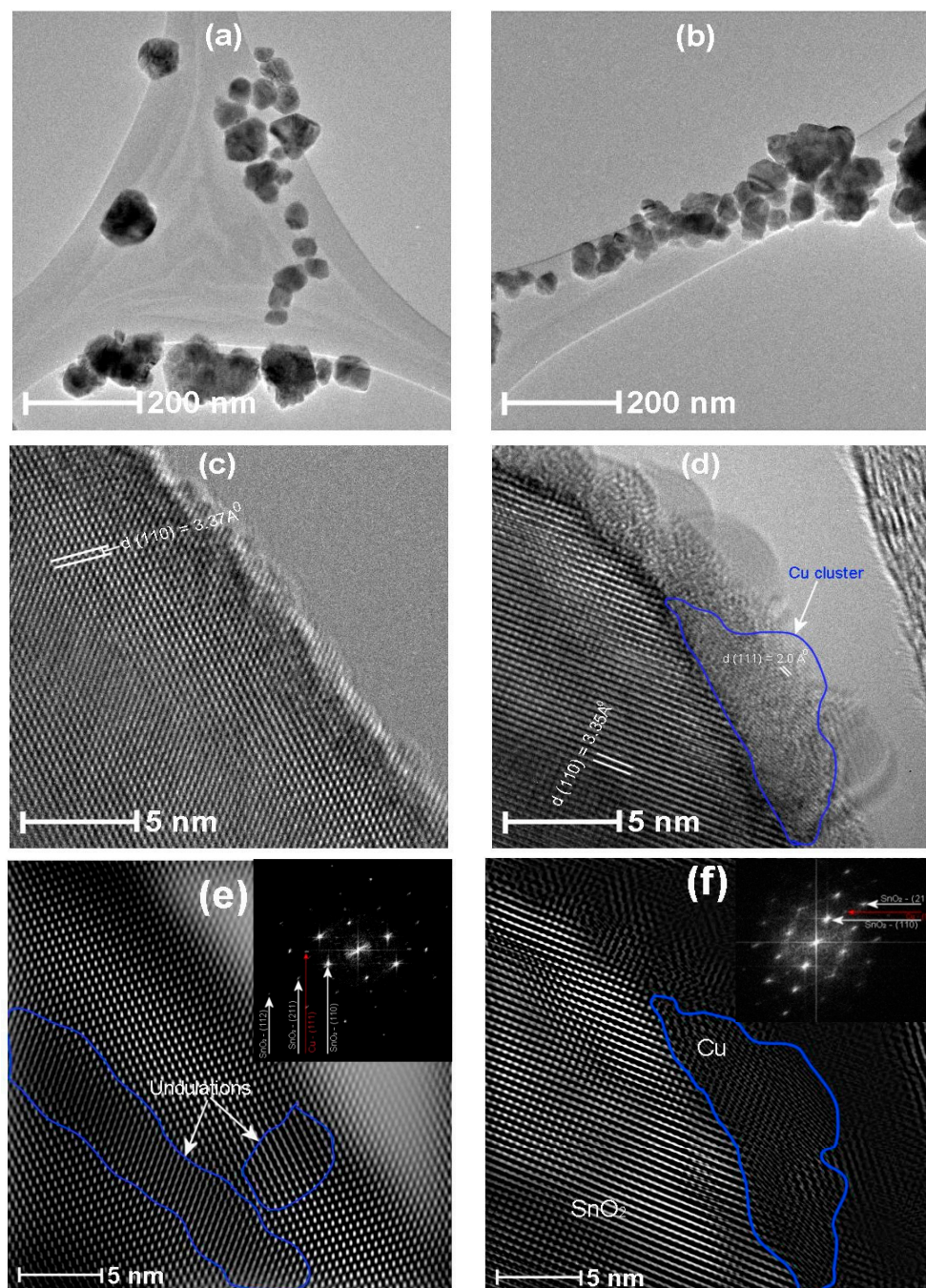


Figure 8. HRTEM images of Cu:SnO₂ prepared by (a) chemical doping with urea as precipitation agent; (b) impregnation with ammonia as precipitation agent; a higher magnification of surface of SnO₂ crystal surface of (a,b) is shown in (c,d). (e) Reconstructed HRTEM image after masking of (c); inset: the corresponding SAED pattern, and (f) reconstructed HRTEM image after masking of (d); inset: the corresponding SAED pattern.

Cu doping localized on the surface of the SnO₂ particle was observed for the impregnated powders (Figure 8d,f), marked in the blue region. Also, no defects were founded in the SnO₂ crystal. The inter-plane distance measured for the copper particle corresponds to the (111) plane of cubic Cu (JCPDS Card 00-004-0836) [55], which confirms that the cluster formation of the dopants takes place on the surface of the SnO₂, which assures the possibility of a spillover mechanism in the gas sensing properties.

Contrarily, for chemically doped powders, no clusters of dopants were observed on the surface but the surface undulations produced by doping were observed and are marked in Figure 8e, highlighted in the blue regions. Therefore, when using the chemical doping method, the dopants are incorporated into the SnO₂ lattice. Moreover, the (110) inter-plane distances were estimated to be 3.35, 3.37 and 3.36 Å for undoped, chemically doped and impregnated powders, respectively. This increase in the lattice parameter suggests an increase of the unit cell volume for the doped powders, which is a cogent evidence for Cu insertion in the host (SnO₂) matrix. The estimated lattice spacing values from the HRTEM are consistent with the calculated XRD data. A comparison of the calculated d-spacing values for all the dopants and doping methods is tabulated in Table 4. The change in the lattice spacing is slightly higher in chemically doped powders, which is consistent with the higher left shift in the (110) diffraction peak (Figure 3).

Table 4. A comparison of estimated d-spacing values for all the dopants and doping methods.

Dopant	SnO ₂ -d (110) in Å					
	Urea	Ammonia	Chemically Doped		Impregnated Powders	
			Urea	Ammonia	Urea	Ammonia
Undoped	3.35853	3.35492	-	-	-	-
Cu	-	-	3.3732	3.36927	3.3682	3.3927
Pt	-	-	3.39422	3.38839	3.3801	3.35427
Pd	-	-	3.41855	3.40501	3.40697	3.35706

Figure 9a shows the surface of the Cu:SnO₂ crystals divided into regions I and II, with their corresponding reconstructed (Figure 9b,c) patterns. Figure 9b,c evidence the stacking faults (marked with red arrows) in the SnO₂ lattice, which are attributed to the Cu doping.

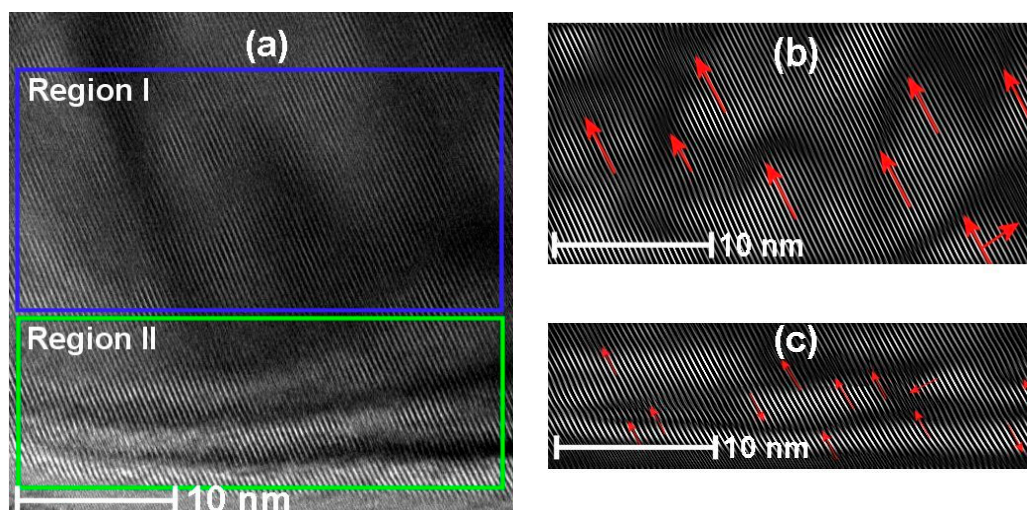


Figure 9. HRTEM images of Cu:SnO₂ using chemical doping with urea as precipitation agent (a) surface of the SnO₂ crystal with stacking faults; (b) reconstructed image of Region I; and (c) reconstructed image of Region II.

In “Region I” from Figure 9 these faults are consistently observed on all surfaces of chemically doped SnO₂ powders. The numbers of defects produced were more in the case of Pt and Pd than with Cu, which is due to the higher ionic radii of Pt and Pd.

Figure 10a,c show the defects produced for the SnO₂ powders chemically doped with Pt and Pd, respectively. FFT reconstructed images in Figure 10a,c are shown in Figure 10b,d, respectively. For Pt doped SnO₂ powders the stacking faults obtained are in the (110) plane surface, which are marked

with red arrows, whereas, in case of Pd:SnO₂ powders, as shown in Figure 10d, the stacking faults or defects are obtained on the {221} facets of SnO₂ projected from (110) plane. The {221} plane is a typical facet of SnO₂ and can be described as a combination of (001) and (110) steps [56].

According to Han et al. [56], {221} facets are very favorable for gas sensing properties. Further detailed chemical analysis of the Pd:SnO₂ crystals is required to explain the reasons for the formation of {221} facets. The calculated (110) inter-plane distance was 3.39 and 3.41 Å for chemically doped Pt and Pd:SnO₂ powders, respectively. The presence of dislocations and stacking faults observed in the HRTEM analysis agrees with the Raman bands of Cu-, Pt- and Pd-doped SnO₂ powders, which show an asymmetric broadening A_{1g} Raman peak (cf. Figure 4b). The internal strain produced due to the doping leads to a downshift and broadening of the A_{1g} Raman peak [57]. Additionally, due to the stacking faults, the crystals obtained have Sn-enriched stoichiometry in addition to Sn-interstitial spaces and oxygen vacancies [58], therefore, the increment in the [Sn]/[O] ratio at the stacking fault causes electronic effects, which increases bulk conductivity and subsequently a CO sensing response.

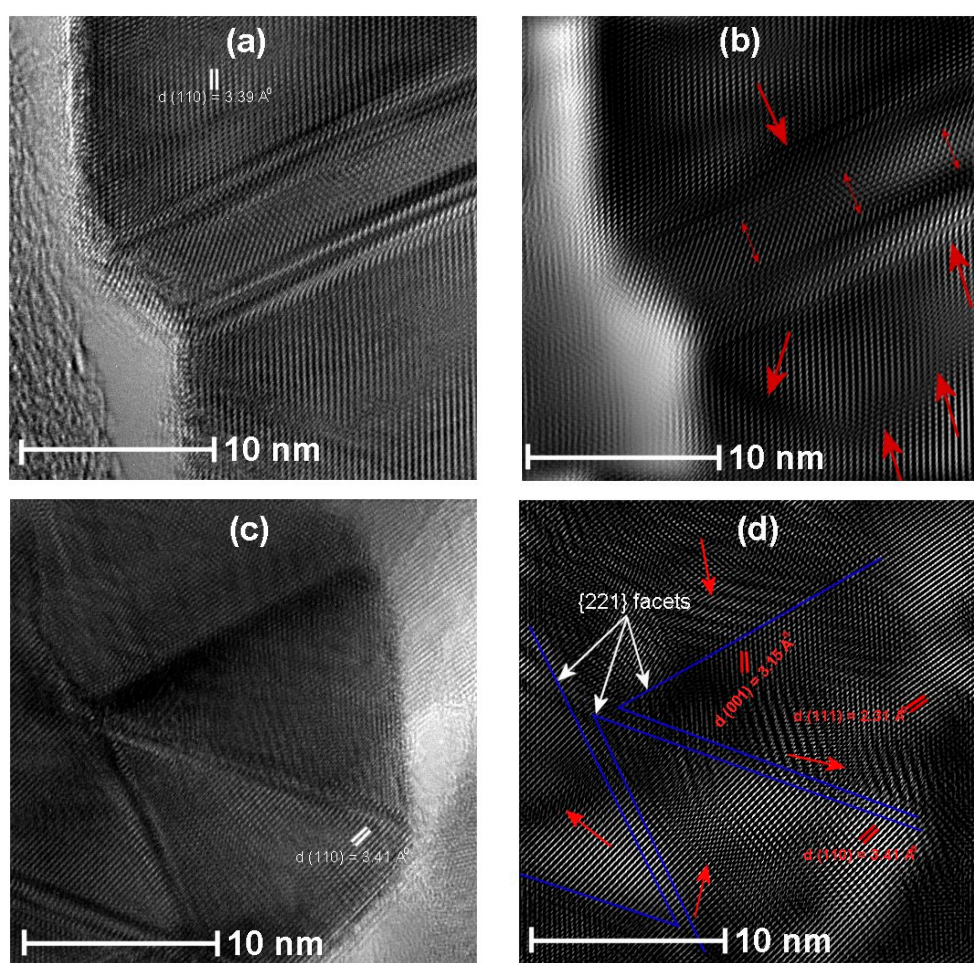


Figure 10. HRTEM images of (a) Pt:SnO₂ prepared by chemical doping with urea as precipitation agent, (b) Reconstructed HRTEM image after masking of (a), (c) Pd:SnO₂ prepared by chemical doping with urea as precipitation agent and (d) Reconstructed HRTEM image after masking of (b).

3.5. CO Sensing Properties

CO gas sensing measurements were performed for the manufactured Cu-, Pt- and Pd-doped SnO₂ pellets to taste their potential applications in chemical sensors. Top and cross sectional views of the gas sensor employed in this work are shown in Figure 11a,b, respectively. To study the effect of precipitation agent, dopants and doping method on the measuring temperature and CO gas

concentration of our SnO₂ samples, the sensor response was tested as a function of CO gas in the range of 1–300 ppm at temperatures of 100, 200 and 300 °C. Figure 12a–d correspond to the CO sensing properties of Cu:SnO₂_U_Chem, Cu:SnO₂_A_Chem, Cu:SnO₂_U_Impe and Cu:SnO₂_A_Impe, respectively. Table 5 summarizes the highest sensing responses obtained at 300 °C for 300 ppm of CO gas concentration, for the different dopants used, synthesis routes and doping methods. The undoped sensing responses are reported from our previous work [34].

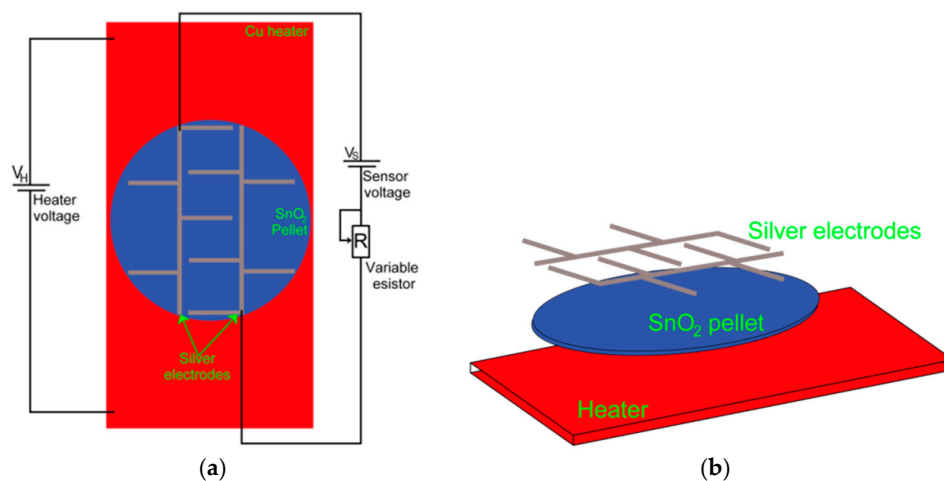


Figure 11. (a) Top view and (b) cross sectional view of SnO₂ sensor.

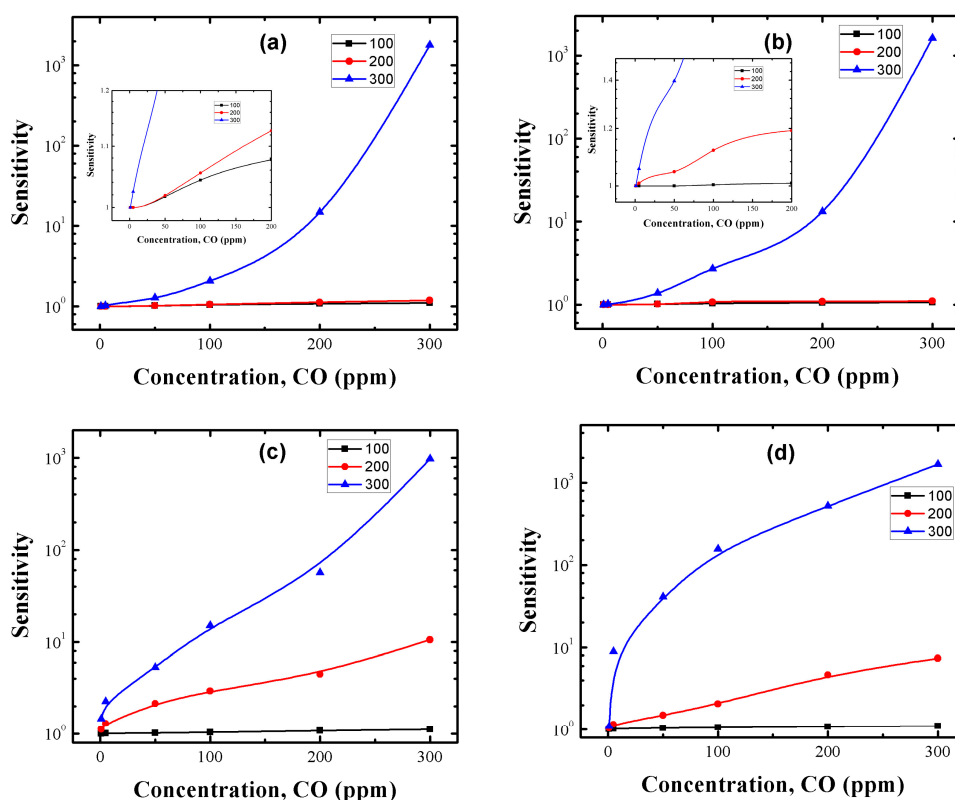


Figure 12. Sensing response of Cu:SnO₂ powders using chemical doping with precipitation agent (a) urea; (b) ammonia and Cu impregnated SnO₂ powders with precipitation agent (c) urea; (d) ammonia.

Table 5. Sensing responses at 300 °C for 300 ppm of CO of the Cu-, Pt- and Pd-doped SnO₂ pellets prepared by different methods.

	Undoped	Cu	Pt	Pd
U_Chem	12	-	-	-
A_Chem	10	-	-	-
U_Chem		1782.609	1200	502.5
A_Chem		1625	721.519	287.6405
U_Impe		1666.667	428.7234	245.4546
A_Impe		975.7412	387.3333	224.1485

Irrespective of the dopant used, doping method and synthesis route employed, the sensing responses of doped SnO₂ pellets are higher than for undoped SnO₂ (Table 5). From Figure 12a–d and Table 5, it can be observed that irrespective of the synthesis route and doping method employed, all the pellets' sensing responses increase with an increment in the gas concentration and measuring temperature.

Cu:SnO₂_U_Chem, Cu:SnO₂_A_Chem, Cu:SnO₂_U_Impe and Cu:SnO₂_A_Impe also exhibits a rapid response increase to reach a maximum value of 1782, 1625, 975 and 1666, respectively, at the measuring temperature of 300 °C. Chemically doped powders show a slight increase in sensing response when measured at 100 and 200 °C (cf. insets of Figure 12a,b), whereas the impregnated powders show an effective sensing response at the measuring temperature of 200 and 300 °C (Figure 12c,d). Finally, only at higher gas concentrations like 300 ppm, do pellets manufactured with urea as precipitation agent show higher sensing responses than powders utilizing ammonia as precipitation agent (Table 5). Additionally, irrespective of the precipitation agent utilized, the sensing responses obtained are higher for impregnated Cu:SnO₂ powders than chemically doped powders at low concentrations (1–50 ppm) and for lower temperatures (200 °C) and the response shows an increasing tendency with an increase in CO concentration, for all the measuring temperatures (Figure 12a,b insets).

To study the effect of the dopant type on the CO sensing responses, the sensor responses of the Pt- and Pd-doped SnO₂ pellets were tested taking into consideration the different doping methods, and results are reported in Figure 13. We can observe that Pt- and Pd-doped pellets are in the sensing response range of the Cu-doped pellets. The sensing responses increase with respect to temperature and gas concentration for both Pt- and Pd-doped samples. Additionally, impregnated powders showed relatively higher sensing responses at lower concentrations (0–50 ppm) and lower temperatures (200 °C). Finally, the sensing responses of Pt- and Pd-doped SnO₂ samples are smaller compared to Cu-doped samples. Chemically doped powders show higher sensing responses than the impregnated ones for all Cu, Pt and Pd:SnO₂ powders (Table 5) at higher CO concentrations and this trend is reversed for lower CO gas concentrations. Table 5 summarizes the sensing responses of the Cu, Pt and Pd:SnO₂ pellets prepared by different doping methods and precipitation agents, measured at 300 °C for 300 ppm of CO. We can observe that Cu shows higher sensing responses than Pt and Pd in each case. The sensing response increases with respect to the measuring temperature and gas concentration. The detailed explanation of the above obtained results and their corresponding reasons will be discussed in the upcoming.

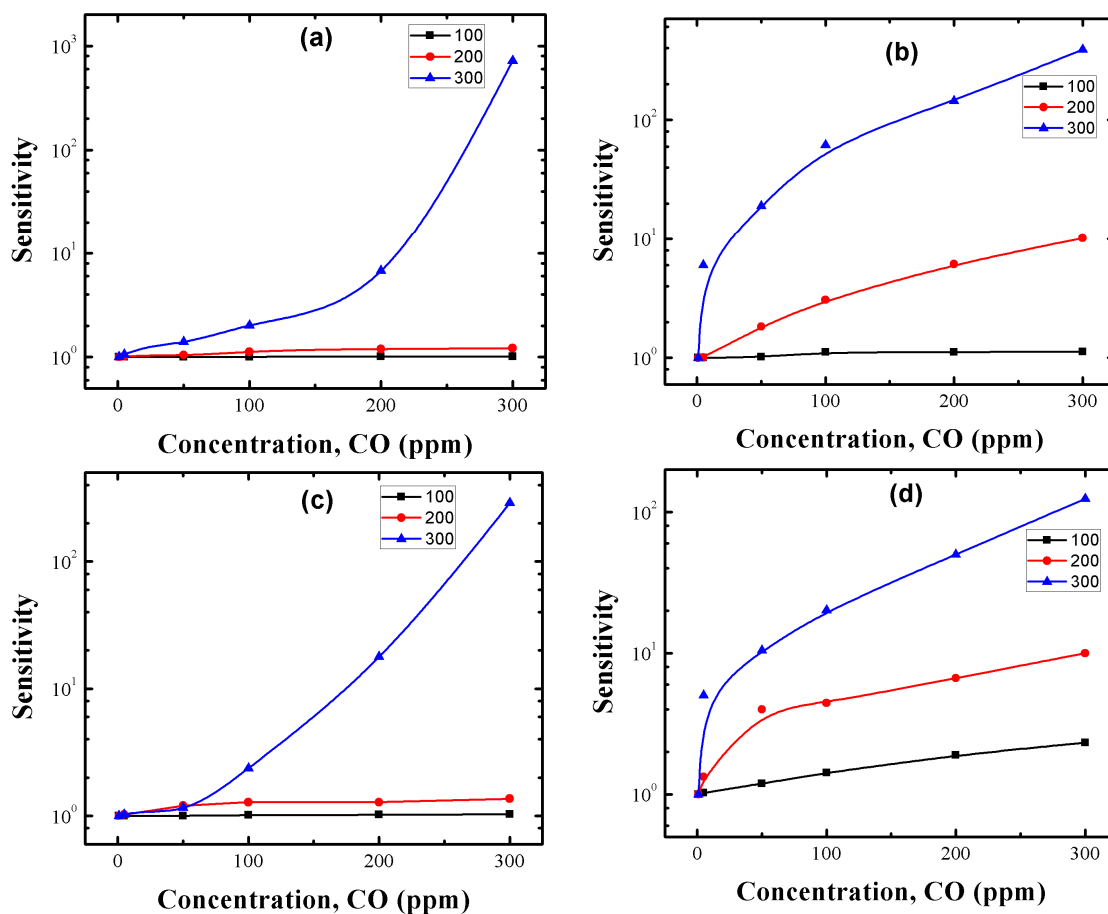


Figure 13. Sensing response of (a,b) Pt:SnO₂ and (c,d) Pd:SnO₂ powders using (a,c) chemical doping and (b,d) impregnation method with urea as precipitation agent.

4. Discussion

Gas-Sensing Mechanism

A description of the oxygen adsorption on a metal oxide with a change in surface conductivity with respect to CO is presented in Figure 14. As the temperature increases, atmospheric oxygen adsorbs on the SnO₂ surface due to its oxygen vacancies which results in the formation of a depletion region between adsorbed oxygen and SnO₂ surface (left column of Figure 14). Later, as the reducing gas interacts with the adsorbed oxygen and increase the conductivity which is measured as a sensor signal (right column of Figure 14).

A rise in the CO gas concentration leads to an increment in the number of reactions with the pellet surface, which in turn increases the magnitudes of conductivity and subsequently the sensing response. Also, the oxygen species adsorbed at temperatures above 300 °C is atomic (O⁻) which is more reactive, whereas the adsorbed oxygen at 100 and 200 °C temperatures is in molecular form (O₂, O₂²⁻) [59]. Therefore, the sensing response increases accordingly to the gas concentration and temperature which is in consistent with our results reported in Figures 12 and 13. From the obtained SEM and HRTEM results, it is evident that the structures obtained are non-spherical and porous, which provides an additional active sites to adsorb more oxygen species which increased the sensing response [60]. Figure 15 indicates the difference between the contact area for spherical and non-spherical contacts. For illustrative purposes, considering that the non-spherical structures formed a tetragon (which is a typical phase of SnO₂), this results in a different contacting form with different contact area.

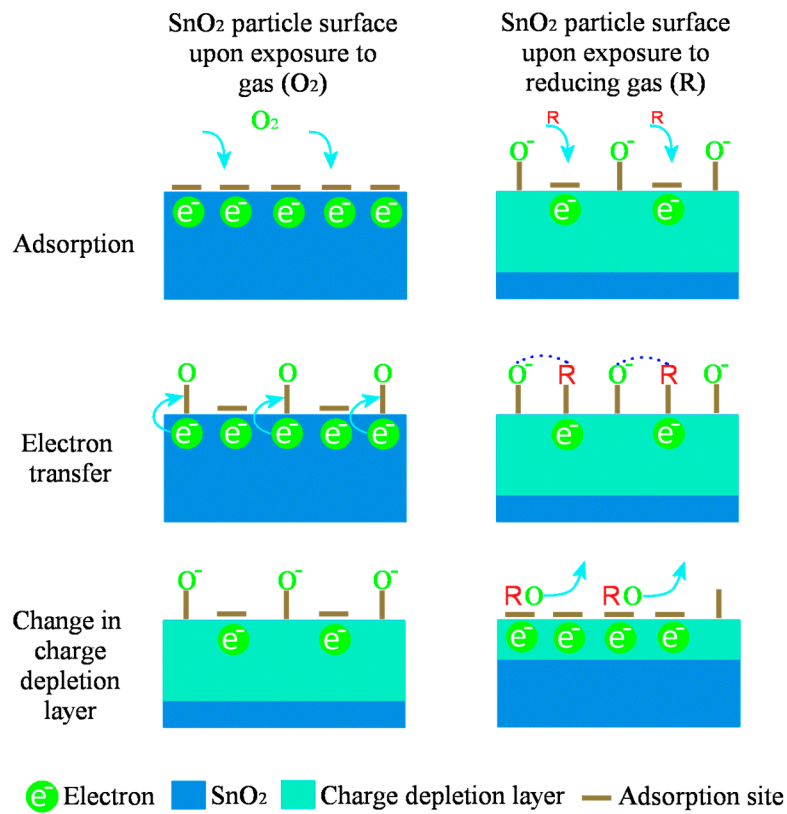


Figure 14. Schematic indicating the sensing mechanism on the SnO₂ surface. Left column indicates reaction with oxygen, whereas right column shows the interaction with reducing gas like CO.

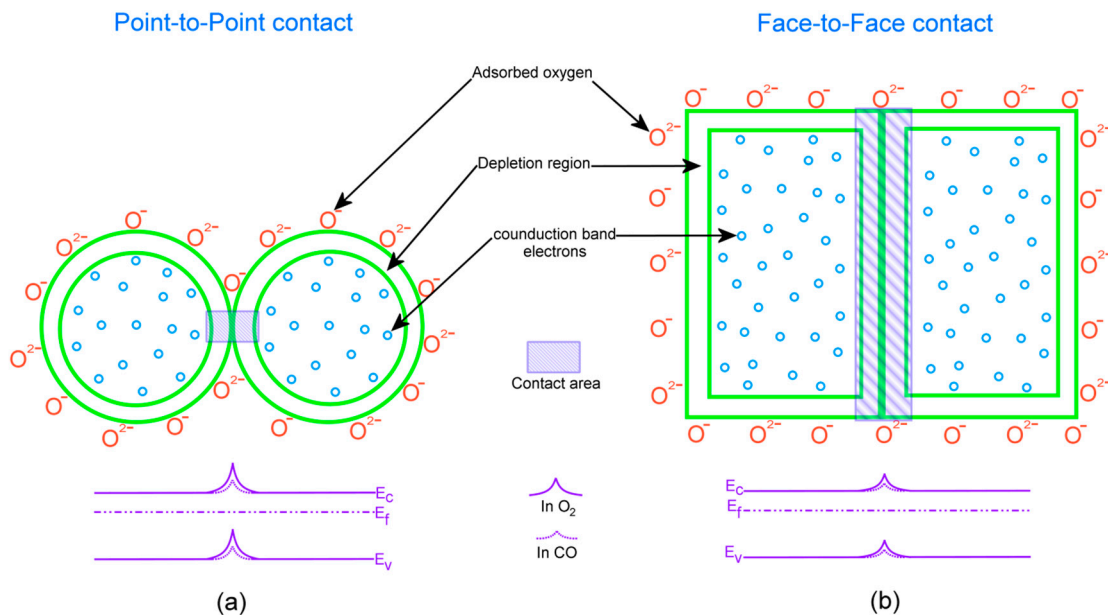


Figure 15. Illustration of the contact area for (a) spherical grains; and (b) tetragonal grains.

As shown in Figure 15a, for spherical structures point-to-point contacting consists of relatively less contact area compared to the tetragonal structures with the face-to-face contact as shown in Figure 15b. When different tetragonal particles are exposed to air, oxygen adsorption between the face-to-face contact results in a less resistive depletion region between the adjacent particles

compared to the point-to-point contact. The face-to-face contacting form of tetragonal particles enhances the surface-depletion control rather than grain boundary barrier control, which results in a higher sensing response.

Compared to the state of art of SnO₂-based sensors [20,25,29,31,51,58,60], the CO sensing response obtained in this work is much higher. A summary of the sensing responses is presented in Table 6. The main aim of comparing sensing responses of different gases and temperatures is to convey the idea that the sensing responses obtained in this work are much higher due to the presence of adequate material resulting from the usage of pellet sensors. The utilization of pellets increased the sensing response values which in the future can served as a reference to compare the responses of thin and thick films sensor. The maximum sensing response obtained for CO was around 100 and for H₂S it was around 357. The minimum operation reported in Table 6 was around 100 °C. In our work, we have obtained an CO sensing response increased by one order of magnitude (1782) for Cu:SnO₂ powders for very low concentrations of CO.

Table 6. Representative synthesis methods, material characteristics, and corresponding sensing responses for SnO₂ based sensors compared to present work.

SnO ₂ Synthesis Method	SnO ₂ Precursor	Crystallite Size (nm)	Sensing Response (Ra/Rg at Specified Operating Temperature and Mole Fraction of Target Gas)	Reference
Vapor–liquid–solid	Sn Powder	~75–90	~80 at 300 °C and at 10 ppm of CO	[61]
Hydrothermal process	SnCl ₂ ·2H ₂ O	~10	~78 at 220 °C and at 100 ppm of acetone	[62]
Hydrolysis and Precipitation	SnCl ₄ ·5H ₂ O	~15	~80 at 350 °C and at 600 ppm of CO	[63]
Chemical spray pyrolysis	SnCl ₄ ·5H ₂ O	~10	~132 at 225 °C and at 400 ppm of NO ₂	[64]
Precipitation	SnCl ₄ ·5H ₂ O	~14	~100 at 350 °C and at 600 ppm of CO	[65]
One-step Solvothermal route	SnCl ₄ ·5H ₂ O	~10	~22.69 at 260 °C and at 50 ppm of ethanol gas	[66]
Sol-Gel	SnCl ₄ ·5H ₂ O	~8–20	~1.95 at 100 °C and at 5 ppm of CO	[67]
Hydrothermal synthesis	SnCl ₄ ·5H ₂ O	~3.4 ± 0.8 nm	~357 at 100 °C and at 5 ppm of H ₂ S	[68]
Present work	SnCl ₄ ·5H ₂ O	~35	~1782 at 300 °C and at 300ppm	–

For chemically doped powders, the incorporation of additives in the SnO₂ lattice increases the charge carrier concentration, which subsequently increases the bulk conductivity and decreases the thickness of the space charge region. This effect is clearly observed from our SEM results (Figure 5). During the thermal treatment, the presence of dopants gives rise to two important factors, coalescence of the SnO₂ and modification of the crystal structure [17,50].

Due to coalescence, we can observe an increase of the contact area between crystallites and the formation of necks between grains. This will lead to formation of a sensor matrix network [16,69], which is obtained for chemically doped powders. Modification of crystallographic structure leads to an increase in crystal defect concentration and a change in crystallographic faceting, and these changes will enhance the conductivity of the SnO₂ matrix [70,71]. It is evident from the HRTEM results (Figures 8–10) that stacking faults for Cu and Pt:SnO₂ powders and {221} facets for Pd:SnO₂ powders are observed. It was recently shown by Han et al. [56], that {221} facets show higher sensing responses compared to others. Therefore, the formation of necks and the structural modifications produced by chemical doping enhanced the sensing response of the doped SnO₂ pellets. Crystallite size obtained for powders with urea as precipitation agent were relatively uniform and homogeneously distributed, which increased the surface to volume ratio and further the sensing response [72].

The sensing response of the impregnated powders is due to the formation of clusters on the surface of the SnO₂ crystals (Figure 8d,f). Therefore, two types of sensitization mechanisms, chemical and electronic, are considered for explaining the effect of clusters on the sensing response. Detailed explanations of both mechanisms have been discussed by many authors previously [73–75], Figure 16 shows both mechanisms in detail. In the electronic mechanism, there is only electronic interaction between the semiconductor and cluster and these interactions change depending on the form of the cluster. It has been evidenced that metal clusters like Cu, Pt and Pd in oxide form can only interact electronically with the SnO₂ and these interactions vanish if the clusters are metallic [60]. Since no

oxides were observed from our HRTEM results, the electronic mechanism can be ruled out. To the best of our knowledge, until now the previous reports [46,75] suggest that the spillover effect (chemical mechanism) lowers the measuring temperature, which could be the possible reason for the increased sensing response for our impregnated powders at 200 °C (Figures 12 and 13).

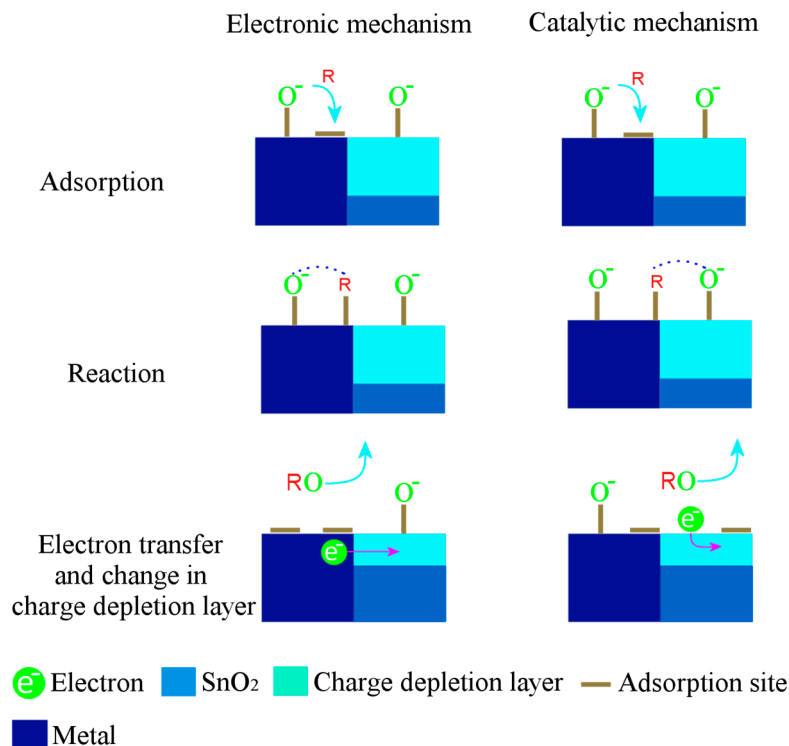


Figure 16. Schematic diagram indicating the general steps involved in the electronic (left column) and catalytic (right column) mechanisms active in SnO_2 sensors with metal additives. R represents a reducing gas.

Another parameter observed from Figures 12 and 13 is that Cu, Pt and Pd: SnO_2 powders present higher sensing responses for chemically doped samples only at higher CO concentrations (100–300 ppm). Impregnated powders show higher sensing responses for low CO concentrations (0–50 ppm). This shows that the impregnated powders show an exponential increase and a saturation tendency with increased gas concentration, whereas for chemically doped powders no saturation is shown until 300 ppm of CO. Therefore, it can be concluded that the clusters formed in the impregnation method favor the detection of very small concentrations of CO and saturates with lower sensing responses, whereas chemically doped powders require a minimum of 50 ppm of CO for detection, but the response is relatively higher at higher gas concentrations.

Another crucial factor that influences the sensing response is the doping concentration of the additives. In this work, we have utilized 1 wt % of concentration for all samples. It has been established that the response of SnO_2 -based sensors lies in the range of 0.1–0.6% [41] for noble metals and for the transition metals it is in the range of 1–4% [48]. However, as we observe from the results obtained in this work, we can conclude that the sensing response depends on many factors like the measuring temperature, microstructure, crystallite size and shape, dopants and on the interaction between the sensing matrix and gas molecules. Further work is necessary to find the exact role of transition and noble metals as dopants on the CO sensing response. A comparison of doping methods and precipitation agents utilized in this work, with their corresponding advantages and sensing responses for only higher CO concentrations of Cu: SnO_2 pellets was represented graphically in Figure 17. Lower gas concentrations shown are not well understood due to a very different behavior with respect

to the doping methods utilized. A more detailed study will be performed in our future work to determine the effect of gas concentration on the doping method. From Table 5, irrespective of the doping method and synthesis route, Cu as dopant showed higher sensing responses than Pt and Pd, which is an interesting and novel result. Therefore, doping of Cu, a transition metal, in SnO₂ powders at 1 wt % doping produced better sensing response magnitudes in this work than noble metal dopants like Pt and Pd. From this result, it can be concluded that the fabrication of Cu:SnO₂ sensors will be a relatively cost effective design method, while featuring a higher CO sensing response magnitude.

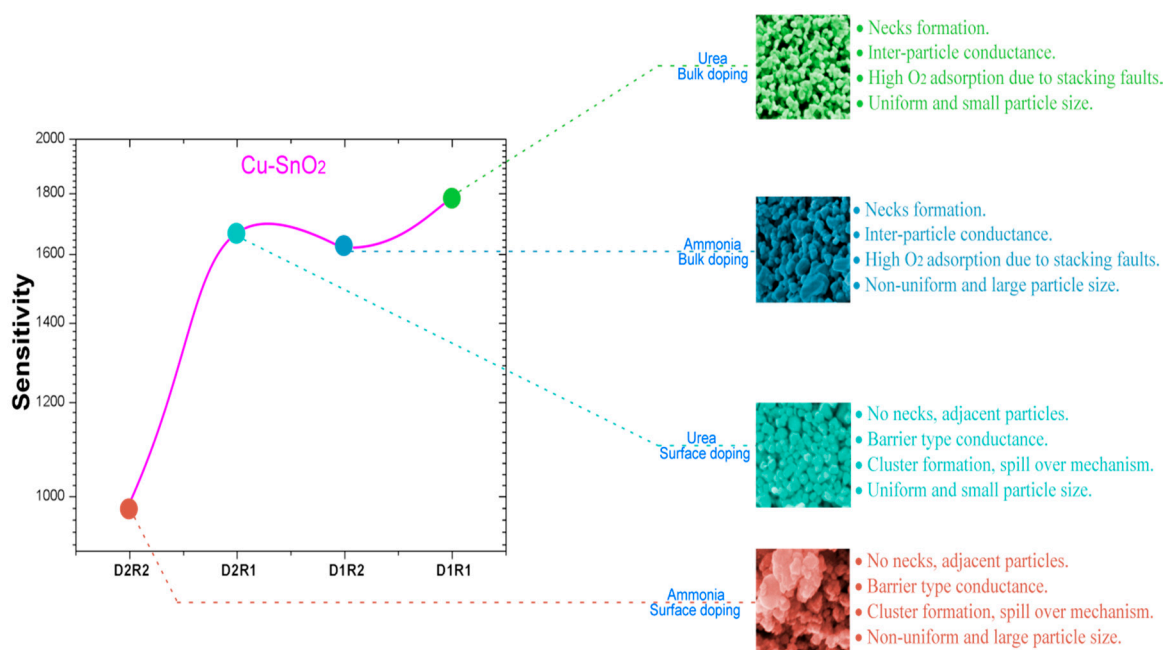


Figure 17. Graphical comparison of synthesis methods of Cu:SnO₂ pellets with corresponding intellects for achieving the high sensing responses for higher CO concentrations (0–300 ppm).

5. Conclusions

In this work, Cu-, Pt- and Pd-doped SnO₂ powders were successfully synthesized utilizing chemical doping and impregnation methods. Cu-, Pt- and Pd-doped SnO₂ powders crystallite size and porosity was increased, respectively, compared to the undoped powders, due to the increase in the ionic radii of the dopants. A shift in the (110) SnO₂ plane confirms the incorporation of dopants in the SnO₂ crystal lattice. The intensity of the Raman peaks decreased in the order of undoped, Cu, Pt and Pd:SnO₂. This decrease corresponds to the amount of extraction and compression of Sn-O bonds inside the lattice. Particle sizes obtained by SEM were around 25–35 nm for all the Cu-, Pt- and Pd- doped powders. HRTEM analysis of dopant positions confirms the stacking faults and cluster formation for the powders obtained by chemical doping and impregnation, respectively. Sensing responses of Cu:SnO₂ powders are much higher compared to Pt and Pd:SnO₂ powders. A drastic decrease in the crystal quality and a substantial number of defects for Pt and Pd:SnO₂ powders reduced their sensing responses in comparison with Cu:SnO₂ powders. Irrespective of the doping method, pellets manufactured from the powders synthesized utilizing urea showed high sensing responses than those synthesized using ammonia. Additionally, chemically doped sample sensing responses are higher than impregnated ones. The face-to-face contact form of tetragonal particles enhances the surface-depletion control rather than grain boundary barrier control, which results in a high sensing response in Cu:SnO₂ powders. The maximum sensing responses obtained was for Cu-doped pellets and was around 1782 for powders incorporated by the chemical method with urea as precipitation agent.

Acknowledgments: The authors acknowledge the conacyt for the post doctoral funding through SENER-Hydrocarbons project and this work was also supported and funded by “Universidad Autonoma del Estado de Hidalgo”.

Author Contributions: Conceived and designed the experiments: Venkata Krishna Karthik Tangirala, M. Olvera. Performed the experiments: Venkata Krishna Karthik Tangirala. Analyzed the data: Venkata Krishna Karthik Tangirala, M. Olvera, Ventura Rodríguez Lugo, Heberto Gómez Pozos. Wrote the paper: Venkata Krishna Karthik Tangirala, M. Olvera, Heberto Gómez Pozos and Ventura Rodríguez Lugo.

Conflicts of Interest: The authors declare no conflict of interest.

References

1. Orozco, L. Gas Detectors: Analog Dialogue: Analog Devices 2015. Available online: <http://www.analog.com/en/analog-dialogue/articles/designing-low-power-toxic-gas-detector.html> (accessed on 28 April 2017).
2. Vetter, S.; Haffer, S.; Wagner, T.; Tiemann, M. Nanostructured Co_3O_4 as a CO gas sensor: Temperature-dependent behavior. *Sens. Actuator B Chem.* **2015**, *206*, 133–138. [CrossRef]
3. Ciureanu, P.; Middelhoek, S. *Thin Film Resistive Sensors*, 1st ed.; Institute of Physics: Philadelphia, PA, USA, 1992; pp. 232–345.
4. Marc, J.M.; Morrison, S.R. *Chemical Sensing with Solid State Devices*, 1st ed.; Harcourt Brace Jovanovich: London, UK, 2012; pp. 479–516.
5. Yamazoe, N.; Fuchigami, J.; Kishikawa, M.; Seiyama, T. Interactions of tin oxide surface with O_2 , H_2O and H_2 . *Surf. Sci.* **1979**, *86*, 335–344. [CrossRef]
6. Heiland, G. Homogeneous semiconducting gas sensors. *Sens. Actuator* **1981**, *2*, 343–361. [CrossRef]
7. Morrison, S.R. Semiconductor gas sensors. *Sens. Actuator* **1981**, *2*, 329–341. [CrossRef]
8. Naoyoshi, T. Gas-Detecting Device. U.S. Patent 3,631,436, 28 December 1971.
9. Wagner, C. Physical Chemistry of Ionic Crystals Involving Small Concentrations of Foreign Substances. *J. Phys. Chem.* **1953**, *57*, 738–742. [CrossRef]
10. Barth, S.; Hernandez-Ramirez, F.; Holmes, J.D.; Romano-Rodriguez, A. Synthesis and applications of one-dimensional semiconductors. *Prog. Mater. Sci.* **2010**, *55*, 563–627. [CrossRef]
11. Choi, K.J.; Jang, H.W. One-Dimensional Oxide Nanostructures as Gas-Sensing Materials: Review and Issues. *Sensors* **2010**, *10*, 4083–4099. [CrossRef] [PubMed]
12. Huang, X.-J.; Choi, Y.-K. Chemical sensors based on nanostructured materials. *Sens. Actuator B Chem.* **2007**, *122*, 659–671. [CrossRef]
13. Mathur, S.; Ganesan, R.; Grobelsek, I.; Shen, H.; Ruegamer, T.; Barth, S. Plasma-Assisted Modulation of Morphology and Composition in Tin Oxide Nanostructures for Sensing Applications. *Adv. Eng. Mater.* **2007**, *9*, 658–663. [CrossRef]
14. Gas'kov, A.M.; Rumyantseva, M.N. Nature of Gas Sensitivity in Nanocrystalline Metal Oxides. *Russ. J. Appl. Chem.* **2001**, *74*, 440–444. [CrossRef]
15. Zhang, S.; Sun, D.; Fu, Y.; Du, H. Recent advances of superhard nanocomposite coatings: A review. *Surf. Coat. Technol.* **2003**, *167*, 113–119. [CrossRef]
16. Korotcenkov, G. Practical aspects in design of one-electrode semiconductor gas sensors: Status report. *Sens. Actuator B Chem.* **2007**, *121*, 664–678. [CrossRef]
17. Korotcenkov, G. Gas response control through structural and chemical modification of metal oxide films: State of the art and approaches. *Sens. Actuator B Chem.* **2005**, *107*, 209–232. [CrossRef]
18. Korotcenkov, G.; Cho, B.K. Thin film SnO_2 -based gas sensors: Film thickness influence. *Sens. Actuator B Chem.* **2009**, *142*, 321–330. [CrossRef]
19. Yang, D. Nanocomposite Films for Gas Sensing. *InTechOpen* **2015**, *1*, 857–882.
20. Camargo, P.H.C.; Satyanarayana, K.G.; Wypych, F. Nanocomposites: Synthesis, structure, properties and new application opportunities. *Mater. Res.* **2009**, *12*, 1–39. [CrossRef]
21. Fang, H.; Miller, T.M.; Magruder, R.H.; Weller, R.A. The effect of strain on the resistivity of indium tin oxide films prepared by pulsed laser deposition. *J. Appl. Phys.* **2002**, *91*, 6194–6196. [CrossRef]
22. Vaishnav, V.S.; Patel, P.D.; Patel, N.G. Indium Tin Oxide thin film gas sensors for detection of ethanol vapours. *Thin Solid Films* **2005**, *490*, 94–100. [CrossRef]

23. Gorley, P.M.; Khomyak, V.V.; Bilichuk, S.V.; Orletsky, I.G.; Horley, P.P.; Grechko, V.O. SnO₂ films: Formation, electrical and optical properties. *Mater. Sci. Eng. B* **2005**, *118*, 160–163. [[CrossRef](#)]
24. Yoo, K.S.; Park, S.H.; Kang, J.H. Nano-grained thin-film indium tin oxide gas sensors for H₂ detection. *Sens. Actuator B Chem.* **2005**, *108*, 159–164. [[CrossRef](#)]
25. Vasu, V.; Subrahmanyam, A. Physical properties of sprayed SnO₂ films. *Thin Solid Films* **1991**, *202*, 283–288. [[CrossRef](#)]
26. Zhang, G.; Liu, M. Effect of particle size and dopant on properties of SnO₂-based gas sensors. *Sens. Actuator B Chem.* **2000**, *69*, 144–152. [[CrossRef](#)]
27. Korotcenkov, G.; Brinzari, V.; Boris, I. (Cu, Fe, Co, or Ni)-doped tin dioxide films deposited by spray pyrolysis: Doping influence on film morphology. *J. Mater. Sci.* **2008**, *43*, 2761–2770. [[CrossRef](#)]
28. Mädler, L.; Sahm, T.; Gurlo, A.; Grunwaldt, J.-D.; Barsan, N.; Weimar, U.; Pratsinis, S.E. Sensing low concentrations of CO using flame-spray-made Pt/SnO₂ nanoparticles. *J. Mater. Sci.* **2006**, *8*, 783–796. [[CrossRef](#)]
29. Fang, G.; Liu, Z.; Zhang, Z.; Hu, Y.; Ashur, I.A.; Yao, K.L. Preparation of SnO₂-CuO nanocrystalline powders in two different ways by the sol-gel method. *Phys. Status Solidi* **1996**, *156*, 15–22. [[CrossRef](#)]
30. Cirera, A.; Vilà, A.; Diéguez, A.; Cabot, A.; Cornet, A.; Morante, J.R. Microwave processing for the low cost, mass production of undoped and in situ catalytic doped nanosized SnO₂ gas sensor powders. *Sens. Actuator B Chem.* **2000**, *64*, 65–69. [[CrossRef](#)]
31. Song, K.C.; Kang, Y. Preparation of high surface area tin oxide powders by a homogeneous precipitation method. *Mater. Lett.* **2000**, *42*, 283–289. [[CrossRef](#)]
32. Déchamps, M.; Djuričić, B.; Pickering, S. Structure of Zirconia Prepared by Homogeneous Precipitation. *J. Am. Ceram. Soc.* **1995**, *78*, 2873–2880. [[CrossRef](#)]
33. Karthik, T.V.K.; Maldonado, A.; Olvera, M.D.L.L. Synthesis of tin oxide powders by homogeneous precipitation. Structural and morphological characterization. In Proceedings of the 10th International Conference on Electrical Engineering, Computing Science and Automatic Control (CCE), Mexico City, Mexico, 26–28 September 2012; pp. 1–8.
34. Karthik, T.V.K.; Maldonado, A.; Olvera, M.D.L.L. Manufacturing of tin oxide pellets and their application for CO and C₃H₈ gas sensors. In Proceedings of the 2013 10th International Conference on Electrical Engineering, Computing Science and Automatic Control (CCE), Mexico City, Mexico, 30 September–4 October 2013; pp. 402–406.
35. Haines, J.; Léger, J.M. X-ray diffraction study of the phase transitions and structural evolution of tin dioxide at high pressure: Relationships between structure types and implications for other rutile-type dioxides. *Phys. Rev. B* **1997**, *55*, 11144. [[CrossRef](#)]
36. Giri, P.K.; Bhattacharyya, S.; Singh, D.K.; Kesavamoorthy, R.; Panigrahi, B.K.; Nair, K.G.M. Correlation between microstructure and optical properties of ZnO nanoparticles synthesized by ball milling. *J. Appl. Phys.* **2007**, *102*, 093515. [[CrossRef](#)]
37. Patterson, A.L. The Diffraction of X-Rays by Small Crystalline Particles. *Phys. Rev.* **1939**, *56*, 972. [[CrossRef](#)]
38. Cullity, B.D.; Stock, S.R. *Elements of X-ray Diffraction*, 3rd ed.; Pearson: San Francisco, CA, USA, 2001; Volume 3, pp. 294–366.
39. Dar, M.A.; Batoo, K.M.; Verma, V.; Siddiqui, W.A.; Kotnala, R.K. Synthesis and characterization of nano-sized pure and Al-doped lithium ferrite having high value of dielectric constant. *J. Alloys Compd.* **2010**, *493*, 553–560. [[CrossRef](#)]
40. Shannon, R.D. Revised effective ionic radii and systematic studies of interatomic distances in halides and chalcogenides. *Acta Crystallogr. Sect. A Cryst. Phys. Diffr. Theor. Gen. Crystallogr.* **1976**, *32*, 751–767. [[CrossRef](#)]
41. Jarzebski, Z.M.; Marton, J.P. Physical Properties of SnO₂ Materials: I. Preparation and Defect Structure. *J. Electrochem. Soc.* **1976**, *123*, 199–205. [[CrossRef](#)]
42. Traylor, J.G.; Smith, H.G.; Nicklow, R.M.; Wilkinson, M.K. Lattice Dynamics of Rutile 2015. *Phys. Rev. B* **1971**, *3*, 3457. [[CrossRef](#)]
43. Srinivas, K.; Vithal, M.; Sreedhar, B.; Raja, M.M.; Reddy, P.V. Structural, Optical, and Magnetic Properties of Nanocrystalline Co Doped SnO₂ Based Diluted Magnetic Semiconductors. *J. Phys. Chem. C* **2009**, *113*, 3543–3552. [[CrossRef](#)]
44. Katiyar, R.S. Dynamics of the rutile structure. I. Space group representations and the normal mode analysis. *J. Phys. C Solid State Phys.* **1970**, *3*, 1087–1096. [[CrossRef](#)]

45. Wang, W.; Xu, C.; Wang, G.; Liu, Y.; Zheng, C. Synthesis and Raman scattering study of rutile SnO₂ nanowires. *J. Appl. Phys.* **2002**, *92*, 2740–2742. [[CrossRef](#)]
46. Azam, A.; Ahmed, A.S.; Habib, S.S.; Naqvi, A.H. Effect of Mn doping on the structural and optical properties of SnO₂ nanoparticles. *J. Alloys Compd.* **2012**, *523*, 83–87. [[CrossRef](#)]
47. Fliegel, W.; Behr, G.; Werner, J.; Krabbes, G. Preparation, development of microstructure, electrical and gas-sensitive properties of pure and doped SnO₂ powders. *Sens. Actuator B Chem.* **1994**, *19*, 474–477. [[CrossRef](#)]
48. Matsuura, Y.; Takahata, K. Stabilization of SnO₂ sintered gas sensors. *Sens. Actuator B Chem.* **1991**, *5*, 205–209. [[CrossRef](#)]
49. Lifshitz, I.M.; Slyozov, V.V. The kinetics of precipitation from supersaturated solid solutions. *J. Phys. Chem. Solids* **1961**, *19*, 35–50. [[CrossRef](#)]
50. Korotcenkov, G.; Cornet, A.; Rossinyol, E.; Arbiol, J.; Brinzari, V.; Blinov, Y. Faceting characterization of tin dioxide nanocrystals deposited by spray pyrolysis from stannic chloride water solution. *Thin Solid Films* **2005**, *471*, 310–319. [[CrossRef](#)]
51. Liu, Y.; Dong, J.; Liu, M. Well-Aligned “Nano-Box-Beams” of SnO₂. *Adv. Mater.* **2004**, *16*, 353–356. [[CrossRef](#)]
52. Zhong, Z.; Yin, Y.; Gates, B.; Xia, Y. Preparation of Mesoscale Hollow Spheres of TiO₂ and SnO₂ by Templating Against Crystalline Arrays of Polystyrene Beads. *Adv. Mater.* **2000**, *12*, 206–209. [[CrossRef](#)]
53. McAleer, J.F.; Moseley, P.T.; Norris, J.O.W.; Williams, D.E. Tin dioxide gas sensors. Part 1.—Aspects of the surface chemistry revealed by electrical conductance variations. *J. Chem. Soc. Faraday Trans. 1* **1987**, *83*, 1323–1346. [[CrossRef](#)]
54. Martinez, C.J.; Hockey, B.; Montgomery, C.B.; Semancik, S. Porous tin oxide nanostructured microspheres for sensor applications. *Langmuir* **2005**, *21*, 7937–7944. [[CrossRef](#)] [[PubMed](#)]
55. Batzill, M.; Katsiev, K.; Diebold, U. Surface morphologies of SnO₂. *Surf. Sci.* **2003**, *529*, 295–311. [[CrossRef](#)]
56. Han, X.; Jin, M.; Xie, S.; Kuang, Q.; Jiang, Z.; Jiang, Y.; Xie, Z.; Zheng, L. Synthesis of Tin Dioxide Octahedral Nanoparticles with Exposed High-Energy {221} Facets and Enhanced Gas-Sensing Properties. *Angew. Chem.* **2009**, *121*, 9344–9347. [[CrossRef](#)]
57. Alim, K.A.; Fonoberov, V.A.; Shamsa, M.; Balandin, A.A. Micro-Raman investigation of optical phonons in ZnO nanocrystals. *J. Appl. Phys.* **2005**, *97*, 124313. [[CrossRef](#)]
58. Zheng, J.G. Dislocations in nanocrystalline SnO₂ thin films. *Philos. Mag. Lett.* **1996**, *73*, 93–100. [[CrossRef](#)]
59. Lee, J.-H. Gas sensors using hierarchical and hollow oxide nanostructures: Overview. *Sens. Actuator B Chem.* **2009**, *140*, 319–336. [[CrossRef](#)]
60. Kim, H.-J.; Lee, J.-H. Highly sensitive and selective gas sensors using p-type oxide semiconductors: Overview. *Sens. Actuators B Chem.* **2014**, *192*, 607–627. [[CrossRef](#)]
61. Choi, S.-W.; Katoch, A.; Sun, G.-J.; Kim, J.-H.; Kim, S.-H.; Kim, S.S. Dual Functional Sensing Mechanism in SnO₂–ZnO Core–Shell Nanowires. *ACS Appl. Mater. Interfaces* **2014**, *6*, 8281–8287. [[CrossRef](#)] [[PubMed](#)]
62. Wang, X.; Wang, Y.; Tian, F.; Liang, H.; Wang, K.; Zhao, X.; Lu, Z.; Jiang, K.; Yang, L.; Lou, X. From the Surface Reaction Control to Gas-Diffusion Control: The Synthesis of Hierarchical Porous SnO₂ Microspheres and Their Gas-Sensing Mechanism. *J. Phys. Chem. C* **2015**, *119*, 15963–15976. [[CrossRef](#)]
63. Ma, N.; Suematsu, K.; Yuasa, M.; Shimano, K. Pd Size Effect on the Gas Sensing Properties of Pd-Loaded SnO₂ in Humid Atmosphere. *ACS Appl. Mater. Interfaces* **2015**, *7*, 15618–15625. [[CrossRef](#)] [[PubMed](#)]
64. Kumar, M.; Kumar, A.; Abhyankar, A.C. Influence of Texture Coefficient on Surface Morphology and Sensing Properties of W-Doped Nanocrystalline Tin Oxide Thin Films. *ACS Appl. Mater. Interfaces* **2015**, *7*, 3571–3580. [[CrossRef](#)] [[PubMed](#)]
65. Ma, N.; Suematsu, K.; Yuasa, M.; Kida, T.; Shimano, K. Effect of Water Vapor on Pd-Loaded SnO₂ Nanoparticles Gas Sensor. *ACS Appl. Mater. Interfaces* **2015**, *7*, 5863–5869. [[CrossRef](#)] [[PubMed](#)]
66. Sun, Z.P.; Liu, L.; Zhang, L.; Jia, D.Z. Rapid synthesis of ZnO nano-rods by one-step, room-temperature, solid-state reaction and their gas-sensing properties. *Nanotechnology* **2006**, *17*, 2266–2270. [[CrossRef](#)]
67. Lian, Y.; Liu, S.; Hu, Q. Sensors for carbon monoxide based on Pd/SnO₂/CNT nanocomposites. *Phys. Status Solidi* **2014**, *211*, 2729–2734.
68. Chen, Y.; Ma, J.; Mei, L. Gas Sensing of SnO₂ Nanocrystals Revisited: Developing Ultra-Sensitive Sensors for Detecting the H₂S Leakage of Biogas. *Sci. Rep.* **2014**, *4*, 1–8.
69. Korotcenkov, G. Metal oxides for solid-state gas sensors: What determines our choice? *Mater. Sci. Eng. B* **2007**, *139*, 1–23. [[CrossRef](#)]

70. Wang, N.; Cai, Y.; Zhang, R.Q. Growth of nanowires. *Mater. Sci. Eng. R Rep.* **2008**, *60*, 1–51. [[CrossRef](#)]
71. Gryaznov, V.G.; Trusov, L.I. Size effects in micromechanics of nanocrystals. *Prog. Mater. Sci.* **1993**, *37*, 289–401. [[CrossRef](#)]
72. Mulla, I.S.; Ramgir, N.S.; Hwang, Y.K.; Chang, J.-S. Semiconductor Tin Oxide Gas Sensors: From Bulk to Thin Films. *J. Ind. Eng. Chem.* **2004**, *10*, 1242–1256.
73. Brinzari, V.; Korotcenkov, G.; Schwank, J.; Boris, Y. Chemisorptional approach to kinetic analysis of SnO₂: Pd-based thin film gas sensors. *J. Optoelectron. Adv. Mater.* **2002**, *4*, 147–150.
74. Kolmakov, A.; Chen, X.; Moskovits, M. Functionalizing Nanowires with Catalytic Nanoparticles for Gas Sensing Application. *J. Nanosci. Nanotechnol.* **2008**, *8*, 111–121. [[CrossRef](#)] [[PubMed](#)]
75. Matsushima, S.; Maekawa, T.; Tamaki, J.; Miura, N.; Yamazoe, N. New methods for supporting palladium on a tin oxide gas sensor. *Sens. Actuator B Chem.* **1992**, *9*, 71–78. [[CrossRef](#)]



© 2017 by the authors. Licensee MDPI, Basel, Switzerland. This article is an open access article distributed under the terms and conditions of the Creative Commons Attribution (CC BY) license (<http://creativecommons.org/licenses/by/4.0/>).